Meridional Overturning and Heat Transport From Argo Floats Displacements and the Planetary Geostrophic Method (PGM): Application to the subpolar North Atlantic

Alain Colin de Verdière, Thomas Meunier, Michel Ollitrault

JGR Oceans

RESEARCH ARTICLE
10.1029/2018JC014565

Key Points:
- A new direct method to estimate absolute circulation from Argo float displacements and temperature-salinity from World Ocean Atlas
- The method also allows to estimate overturning stream function and meridional heat transport; it is applied in the subpolar North Atlantic

Meridional Overturning and Heat Transport From Argo Floats Displacements and the Planetary Geostrophic Method (PGM): Application to the subpolar North Atlantic

Alain Colin de Verdière[1], Thomas Meunier[2], and Michel Ollitrault[1]

[1]Laboratoire d'Océanographie Physique et Spatiale (LOPS), Infremer Université Brest, CNRS, IRD, Plouzane, France, [2]Department of Physical Oceanography, Ensenada Center for Scientific Research and Higher Education, CICESE, Ensenada, Mexico

Correspondence to:
A. Colin de Verdière,
acolindv@univ-brest.fr

Citation:
Colin de Verdière, A., Meunier, T., & Ollitrault, M. (2019). Meridional overturning and heat transport from Argo floats displacements and the Planetary Geostrophic Method (PGM): Application to the subpolar North Atlantic. *Journal of Geophysical Research: Oceans*, *124*, 6270–6285. https://doi.org/10.1029/2018JC014565

Received 29 NOV 2018
Accepted 2 JUL 2019
Accepted article online 6 JUL 2019
Published online 30 AUG 2019

Abstract A direct method is presented to obtain the meridional overturning and heat transport in oceanic basins from observations under the sole assumptions of geostrophy and hydrostatics. The method is made possible because of the rising Argo float displacements database that can provide a reference level at 1000 dbar for the time mean circulation at 1° × 1° resolution. To achieve the overturning and heat transport objectives, the absolute geostrophic time mean circulation must have nondivergent barotropic transports and this requires the solutions of two Poisson equations with suitable boundary conditions, one for the geopotential at 1000 dbar and one for the barotropic stream function. Applied to the subpolar Atlantic for the period 2000–2009, an overturning of 16–18 Sv is found around 40–50°N, and a meridional heat transport of 0.59 petawatt (PW, 1 PW = 10^{15} W) is found at 40°N (0.23 PW at 60°N) so that on average ~50 W/m^2 is exported from ocean to atmosphere to feed the atmospheric storm track. The zonally averaged flow (the overturning) falls short of explaining the observed heat transport, and the barotropic component of the circulation accounts for up to 50% of the heat transport poleward of 55°N. With the rising Argo float database, the method offers high potential to reconstruct the World Ocean time mean circulation and its heat transport away from the equator at higher resolution. The drawback is that it requires in some critical places additional current observations on the shallow shelves that are not sampled by the Argo floats.

1. Introduction

The net radiation at the top of the atmosphere is not uniform, the earth gaining heat equatorward of 35° latitude and losing it beyond that. Fluid motions in the atmosphere and ocean transport this excess heat from low to high latitudes and the upper atmosphere radiation data gives a maximum transport around 5.5 petawatt (PW, 1 PW = 10^{15} W, Trenberth & Solomon, 1994). The partition of this total between the atmospheric and oceanic contributions remains a long standing issue in our understanding of climate. The high sampling of the observations of the atmosphere allows assimilation models to reconstruct the atmospheric circulation whose heat transport accounts for about two thirds of the total, the difference being attributed to the ocean (Trenberth & Caron, 2001; Trenberth & Solomon, 1994). But such an indirect method for oceanic transport suffers from the errors in the radiation field (~10 W/m^2) and in atmospheric models that impact directly the oceanic contribution. Given the importance of the subject, specific methods have therefore been developed long ago to find out directly the oceanic contribution from in situ observations. The first method uses the observations of surface heat fluxes at the air-sea interface that matches the divergence of time mean oceanic heat transport. However, the errors in the mean air-sea fluxes remain large of the order of 30 W/m^2 and specific methods had to be developed to circumvent the difficulties (see Josey et al., 1999; Large & Yeager, 2009). The second method makes use of observations of the oceanic interior along zonal, transoceanic, quasi-synoptic, hydrographic sections. The geostrophic velocity normal to a section is obtained up to a constant, the so called reference velocity and heat transport at the latitude of the section is simply the area integral of the product of velocity and potential temperature. The difficulty of course is that the reference velocity is unknown so that an accurate determination of heat transport becomes a matter of quantifying the oceanic circulation itself as pointed out by Bryden and Imawaki (2001). The lack of observations of the reference velocity has motivated several ideas. At 24°N the transport of the Florida Current is rather well known, and Hall and Bryden (1982) showed how that transport constrained the reference velocity in the interior

and the net heat transport at that latitude, a method repeated in the Pacific by Bryden et al. (1991). Inverse modeling introduced in oceanography by Carl Wunsch constrained the reference velocity by adding various global conservation laws such as volume transport, salt and nutrients transport, the pending difficulty being that the number of the constraints is much less than the number of unknowns (the reference velocities at each pair of stations over the hydrographic section). In order to remove that indeterminacy, inverse models minimize the distance to an initial guess of the circulation, a guess that remains a subjective choice (Wunsch, 1978, 1996). The numerous sections of the World Ocean Circulation Experiment (WOCE) hydrographic program supplemented by boundary current arrays were carried out with the ultimate objective of observing heat transport, with inverse modeling in mind to find the reference level. Heat and volume transports for the global ocean were found in this manner by Ganachaud and Wunsch (2000), Lumpkin and Speer (2007); MacDonald and Wunsch (1996), and many others in specific basins. As a complement to inverse modeling, direct observations of the reference velocity have been added at key locations along the section, for example, the RAPID program along the 26°N Atlantic section (Johns et al., 2011) and the OVIDE section between Lisbon and Cape Farewell (Mercier et al., 2015). Informative reviews of oceanic heat transport issues have been written by Bryden and Imawaki (2001) and Macdonald and Baringer (2013).

During the 20 years from the Mid-Ocean Dynamics Experiment to WOCE the float technology has improved regularly: the acoustic floats discovered first the turbulent diffusion of the mesoscale eddy field and mapped the eddy kinetic energy of important basins. Under the leadership of Russ Davis, the mapping of the mean circulation became the central focus during the 1990s with the development of the Autonomous Lagrangian Circulation Explorer float (Davis, 1991; Davis et al., 1992). The Autonomous Lagrangian Circulation Explorer float drifts at some chosen depth (~1,000 m), surfaces every so often (~10 days) to acquire a satellite fix of position, and dives back to its target depth. In the absence of acoustic positioning, the mapping of the eddies is abandoned but the displacement of the float over 10 days still gives an unaliased value of the mean velocity over that period. The Argo Float Program launched in 2000 (and continuing to this day) ensures a global coverage of the ocean of the reference velocity averaged over float displacements (Argo, 2000). The present paper summarizes how this new information allows the determination of the mean reference velocity from suitable averages of float displacements and thereby the meridional heat transports over a whole oceanic basin. Several difficulties have been surmounted in previous papers (Ollitrault & Colin de Verdière, 2014, OCV]; Colin de Verdière & Ollitrault, 2016, CVO]), but the importance of the heat transport objective and the novelty of the method justifies a unified presentation for the benefit of the reader. Several issues are also further developed in the present paper. The first step is to transform the Argo velocities to obtain the geopotential at the reference level. This is necessary because the Argo velocities averaged over a Eulerian grid have a large divergent component and therefore cannot be considered geostrophic even though individual 10-day float displacements are probably closely geostrophic. These divergent velocities are filtered out by calculating the geopotential from the observed velocities. While it is easy to derive geostrophic velocities from the geopotential, the inverse operation requires the solution of a Poisson equation over the whole domain under consideration. Once this is done, geostrophic velocities are derived from the geopotential. Because temperature (salinity) measured by the Argo floats is limited to depths less than 2000 db, the World Ocean Atlas 2009 climatology is used instead to compute density over the whole water column. Hydrostatics allows to obtain the absolute geopotential and geostrophic velocities at all depths. The traditional method of determination of heat transport decomposes the velocity field into a barotropic and a baroclinic component, the barotropic being defined as the top to bottom integral of horizontal velocity and the baroclinic as the deviation thereof (Bryan, 1962; Hall & Bryden, 1982). While the baroclinic component is obtained very simply from temperature and salinity fields via the thermal wind, a second difficulty arises because the barotropic flow is divergent and a heat transport calculation is meaningful only with top to bottom mass conservation under a steady state assumption. To obtain these nondivergent barotropic transports, a second Poisson equation must be inverted to find the barotropic stream function. Once absolute geostrophic velocities with nondivergent barotropic transports are known, the meridional overturning circulation (MOC) and the heat transport follow. Given the underlying dynamics, we suggest the name PGM (Planetary Geostrophic Method) to summarize the overall procedure. When comparing the PGM with inverse models and assimilation models (e.g., the ECCO-GODAE of Stammer et al., 2002 and Stammer et al., 2003), the merit of the PGM comes from using only oceanic observations and the geostrophic

assumption. Since the PGM solution is fully determined, there is no need to specify arbitrary initial guesses of the circulation and to minimize errors there from. The planetary geostrophic equations (or thermocline equations) are well known in ocean modeling (Pedlosky, 1996) but to our knowledge have not yet been used to reconstruct heat transports or overturning in an oceanic basin from observations.

The PGM method is described in section 2 with the subpolar North Atlantic taken as a case study to illustrate the method. Overturning and oceanic heat transport for that basin are discussed in section 3.

2. Presentation of the PGM

We illustrate the method in the subpolar gyre of the North Atlantic, a domain limited by 34.5–65.5°N and 85.5–1.5°W that contains 2,720 grid cells of 1° × 1°. We exclude the subtropical gyre from the discussion because the float observations do not resolve well the Gulf Stream system due to the complicated geometry of the Gulf of Mexico, the Florida Straits, and the Blake-Bahama plateau and the lack of data over shallow shelves (the floats do not sample regions shallower than 1000 dbar). The reference velocity at 1000 dbar is obtained from Argo float displacements (the ANDRO database, Ollitrault & Rannou, 2013). The ANDRO data set used herein contains Argo float displacements before 1 January 2010, giving $5.12 \cdot 10^5$ float displacements days found in the [950, 1150] dbar layer with parking times between 4 and 17 days in the subpolar basin. The varying depths of the floats in this narrow range are neglected, the whole data being set to the nominal 1000 dbar level (see Ollitrault & Rannou, 2013 for a discussion of this approximation). Since the floats do not sample areas shallower than 1000 dbar, the absence of information on these shelves is a limit of the present method. These displacements averaged over 1° × 1° bins generate a primary gridded field of Eulerian mean horizontal velocities. Summing the number of float displacements times their parking time in any given bin gives the number of float days used to determine the mean velocity in that bin. On average, 188 float days are found per bin but the distribution is inhomogeneous, a few bins having more than 4 years of data and a few less than 30 days and therefore left empty. This spatial inhomogeneity of the number of float days could be reduced by extending the period beyond 2010, unfortunately the ANDRO data set for the period 2010–2018 has yet to be released. Using raw unchecked data for the later period would not be consistent with the careful and necessary data editing made by Ollitrault and Rannou (2013). To obtain a full depth density field, the World Ocean Atlas 2009 is used, the time period of the float data (2000–2009) being included in the time period of the hydrographic data (Antonov et al., 2010; Locarnini et al., 2010). We now describe the three successive steps of the method.

Step 1: One could expect that the oceanic mean Argo velocities on a uniform grid at a given depth would meet the geostrophic assumptions but they do not. The test is to compute the horizontal divergence of the mean velocity field that should be of the order of velocity/Earth radius under planetary geostrophy. However, the divergence is much larger of order velocity/grid size. Figure 1 shows an example of these time mean Argo float velocities in the Gulf Stream Extension region, a noisy velocity field with a strong divergent component, the amplitude of the horizontal divergence (not shown) being $O(10^{-7}\ s^{-1})$. Even though individual velocities obtained from 10 days float displacements should be close to geostrophic, the Eulerian-mean bin-averaged Argo velocities are not. How to reconstruct a mean geostrophic circulation which could be used for a reference velocity? The geostrophic equations in an isobaric formulation are

$$-fv = -\frac{1}{r_0 \cos\theta}\frac{\partial \Phi}{\partial \lambda} \tag{1a}$$

$$+fu = -\frac{1}{r_0}\frac{\partial \Phi}{\partial \theta} \tag{1b}$$

where λ is longitude, θ is latitude, r_0 is the Earth radius assumed constant (= 6,370 km), and $f = 2\Omega \sin\theta$ is the Coriolis parameter. In this isobaric formulation, the derivatives of the geopotential Φ on the right are carried out at constant pressure. Eliminating the geopotential yields

$$\nabla_H \cdot (f \cdot \mathbf{u}) = 0 \tag{2}$$

with the horizontal divergence given in spherical coordinates by

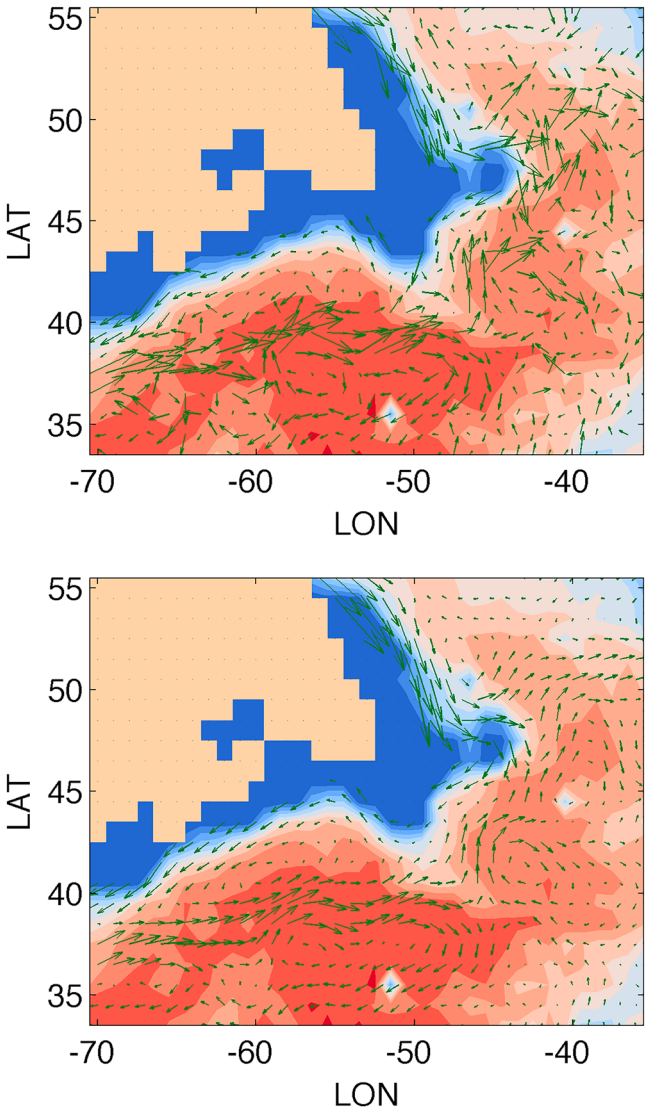

Figure 1. (top) The mean velocity vectors from the ANDRO database at 1000 db over bottom topography (colored shading). (bottom) The geostrophic mean velocities vectors at 1000 db after inversion of the first Poisson problem 4.

$$\nabla_H\cdot(...) = \frac{1}{r_0\ \cos\ \theta}\left[\frac{\partial}{\partial\lambda}(...) + \frac{\partial}{\partial\theta}(\cos\theta...)\right]$$

Expanding the divergence in 2 gives the planetary vorticity equation, one of the cornerstones of large-scale ocean circulation theories (see Pedlosky, 1996):

$$f\ \nabla_H\cdot\mathbf{u}\ +\ \beta v = 0 \tag{3}$$

with $\beta = \frac{2\Omega\ \cos\ \theta}{r_0}$. In this planetary geostrophic approximation, the geostrophic flow on the rotating Earth is divergent but away from the equator; this divergence is rather small of order U/r_0 much smaller than the divergence of the Argo mean velocities. This data-model discrepancy originates from the fact that the mean velocity is computed from an insufficient number of floats in adjacent grid boxes and therefore contaminated by sampling errors of the eddy field due to the small number of degrees of freedom. The way to filter out the noise associated with the divergent part of the velocity field is to calculate the geopotential Φ from the knowledge of the mean velocities $\mathbf{u}$ by taking the divergence of the geostrophic equations (1a) and (1b). By differentiating 1a $\times$ cos θ with respect to λ and 1b with respect to θ, one obtains

$$\frac{\partial^2\Phi}{\partial\lambda^2} + \frac{\partial^2\Phi}{\partial\theta^2} = r_0\left[\frac{\partial(fv\cos\theta)}{\partial\lambda} - \frac{\partial(fu)}{\partial\theta}\right] \tag{4}$$

The Laplacian of the geopotential (in Cartesian coordinates λ, θ) is forced by the underlying vorticity of the flow, actually the curl of the vector $\mathbf{u}^* = (fu, fv\cos\theta)$. Equation (4) is nothing but a special form of the divergence of the horizontal momentum equation, the equation of balance of Charney (1955) adapted here for planetary geostrophic dynamics. Although for flows of velocity scale U and horizontal scale L, the vorticity equation (3) has accuracy limited by $R_\beta = U/\beta L^2$ and the divergence equation (4) is valid to order Rossby number U/fL and is therefore far more accurate than 3. This difference was found by Gent and McWilliams (1983) and is the major justification to use equation (4).

There remains the choice of boundary conditions at the edges of the domain that differs from what is currently done in quasi-geostrophic models. Indeed, in such models when the normal velocity vanishes, the geopotential Φ is constant along the boundary with the unrealistic consequence that there can be no net flow at any depth z in an oceanic basin and therefore no meridional overturning. We choose instead to assume that only the component of the flow tangential to the coast remains geostrophic, a choice in line with the traditional estimates of boundary currents from geopotential differences in a direction normal to the coast. Thus, if $\mathbf{n}$ is the outward unit normal at the edge of the domain and $\mathbf{s}$ is the tangential vector defined by $\mathbf{s} = \mathbf{k}\times\mathbf{n}$, (with $\mathbf{k}$ the upward unit vector), the appropriate geostrophic boundary condition to be used in conjunction with 4 reads

$$\tilde{\nabla}\,\Phi\cdot\mathbf{n} = \mathbf{u}^*\cdot\mathbf{s} \tag{5}$$

with $\tilde{\nabla} = \left(\frac{\partial}{r_0\partial\lambda}, \frac{\partial}{r_0\partial\theta}\right)$.

Boundary condition (5) on the normal derivative of Φ is of the Neumann type and is implemented directly from the *observed* tangential velocity $\mathbf{u}^*.\ \mathbf{s}$. When 4 is integrated over the domain a compatibility condition is found for the Neumann problem and the choice of 5 ensures that this condition is satisfied: so the problem is well posed mathematically. Note that the boundary of the domain is found naturally here either as the coastal

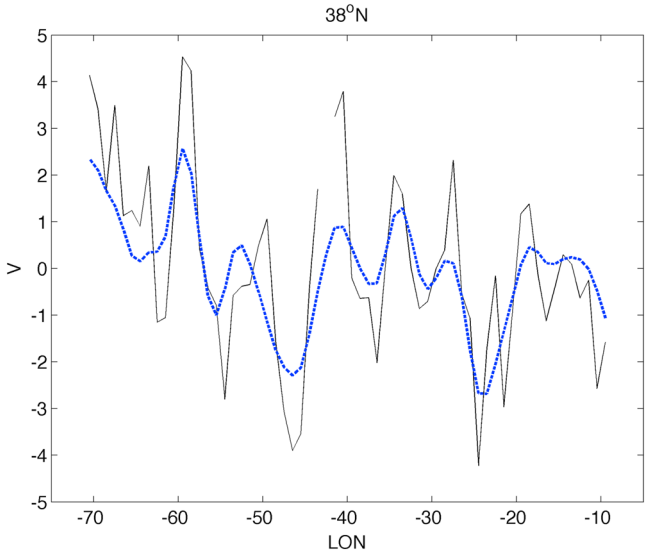

Figure 2. The original Argo mean meridional velocities at 38°N (black line) and the filtered ones, solution of the Poisson equations (4) and (5), (blue dashed line, unit cm/s).

1000-dbar isobath since floats do not sample shallower waters or as the boundary of a data hole if not enough data is present in a region. Given that the velocities normal to the coast do not vanish, the model assumes implicitly the existence of ageostrophic viscous boundary layers to bring the normal velocity to zero at solid boundaries but these cannot be resolved at the coarse resolution used here. The whole method neglects these ageostrophic boundary layers. The various viscous parameterizations of the boundary layers are reviewed by Huck et al. (1999) in the context of prognostic planetary geostrophic models that have been used for the long time integration of the thermohaline circulation at coarse resolution.

The numerical method solving 4 with boundary condition (5) is described in OCV. Once the geopotential Φ is known, the geostrophic velocities $\mathbf{u_G}$ are now recovered from 1, outside an equatorial band, and the divergence 2 vanishes by construction. On the other hand, the vorticity of the initial velocity field and the tangential circulation over the boundary of the domain are left unchanged. The filtering of the divergent motions can be readily appreciated by comparing the raw and the filtered data in Figure 1. The meridional velocity that is central for meridional heat transport is also shown at 38°N before and after filtering (Figure 2). The overall effect of the numerical procedure is to reduce the amplitude of the Argo mean velocities, a reduction that can be quantified over the whole domain. The root-mean-square (rms) of v-v_G (the difference between the original v mean velocity and the geostrophic mean v_G over the domain under consideration) is 1.3 cm/s. Since the rms of v (the original Argo mean velocity signal) is 2.2 cm/s, the rms of the difference amounts to 57% of the original signal, quite a sizable correction. The average over the domain of v-v_G is $-2\ 10^{-2}$ cm/s or 2 orders of magnitude smaller than the rms of the original signal showing that the filtering operation is essentially unbiased.

Once the geopotential is known at a reference level $p_R = 1000$ dbar, we use the World Ocean Atlas (Antonov et al., 2010; Locarnini et al., 2010) to calculate the in situ density from top to bottom on the same horizontal grid. From the knowledge of density, hydrostatics gives the geopotential at any pressure p:

$$\Phi(p) = \Phi(p_R) - \int_{p_R}^{p} dp/\rho \tag{6}$$

Given $\Phi(p)$, the geostrophic relation (1a) and (1b) applied at any pressure p gives the absolute geostrophic velocity everywhere. This geopotential is shown at three depths (surface, 1000 and 2500 dbar) in Figure 3. Errors are due to the insufficient sampling of the Argo velocities in some bins, and a Monte Carlo method was used in OCV (Appendix) to estimate the standard error on the mean geopotential, typically 1–1.5 cm in the subpolar North Atlantic gyre. The surface pattern is a familiar one since it is governed by the density field to a large extent. The Gulf Stream diverges at 45°W with a recirculation to the south and a northern branch following the Grand Banks up to 52°N. That northern stream loses intensity with detaching streamlines moving eastward. The 47°N latitude marks the approximate boundary between the interior south eastward circulation and the North Atlantic Current that reaches the Nordic Seas. The cyclonic coastal circulation in the Labrador Sea animates the western part of the subpolar gyre. The 1000-dbar level (the contribution of the Argo floats velocities) is marked by the northern (cyclonic) and southern (anticyclonic) Gulf Stream recirculations and the anticyclonic Mann eddy at 40°N–40°W (Mann, 1967). The deep North Atlantic drift originates at 50°N with a part recirculating east of the Mid-Atlantic ridge as a southward current (along the ridge). A weak anticyclone is found around the Azores with a cyclonic cell to the East. At 2500 dbar, the deep Gulf Stream recirculations exhibit many similarities with the 1000-dbar surface. The map also shows the injection of Labrador Sea Water (LSW) in the eastern North Atlantic basin around 52.5°N (the Gibbs fracture zone). The net eastward flow of LSW is about 4.5 Sv across 24.5°W in the (1500 dbar, 2500 dbar) depth interval. East of the Mid-Atlantic ridge a southward deep boundary current can be identified with a transport of about 8 Sv at 48.5°N between 25 and 18°W, between 900 db and the bottom. This confirms broadly the inverse modeling results of Paillet and Mercier (1997) and Paillet et al. (1998) who estimated similar LSW injections and pointed out the deep southward current along the ridge.

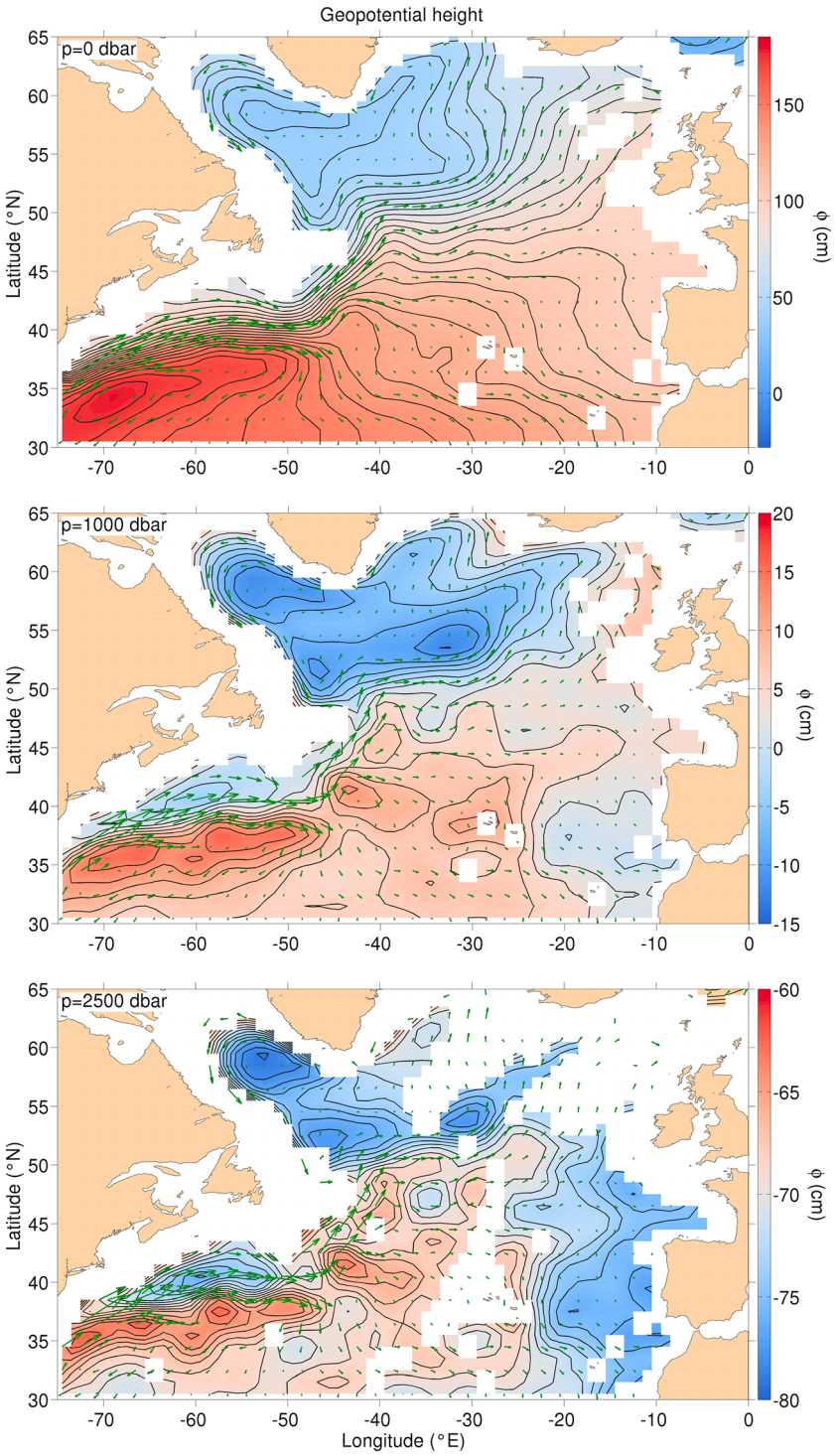

Figure 3. The absolute geopotential height in centimeter at the surface, CI = 5 cm, at 1000 dbar, CI = 2 cm at 2500 dbar, and CI = 1 cm.

Step 2: Under a steady state assumption, the determination of the meridional heat transport in a closed basin such as the North Atlantic requires the net mass transport across any zonal section to vanish (neglecting the small transport from Bering Strait). However, neither the transport of the calculated v_G field nor the meridional Ekman transport meets this requirement. To deal with this constraint

and compute a nondivergent barotropic transport, we proceed as follows. The wind-driven Ekman transport $\mathbf{U_E}$ obeys

$$\rho_0 f\ \mathbf{k}\times\mathbf{U_E} = \boldsymbol{\tau} \tag{7}$$

where $\rho_0 = 1{,}027\ \mathrm{kg/m^3}$ (the mean surface value) and $\boldsymbol{\tau}$ is the wind stress. To compute the Ekman transport, the Large and Yeager (2004) wind stress climatology is used. Note that we neglect bottom dissipation and any bottom Ekman transport. The dynamics governing the geostrophic flow in z coordinates obeys

$$f\ \mathbf{k}\times\rho\ \mathbf{u_G} = -\nabla p \tag{8}$$

with the horizontal ∇ operator now computed at constant z. With a smoothed version of ETOPO2 database used for the bottom depth H, 8 is integrated from $z = -H$ to the surface z = 0, and adding 7, yields the equation for the total barotropic transport:

$$\mathbf{M} = \int_{-H}^{0} \rho\mathbf{u_G}\ \mathrm{d}z + \rho_0\mathbf{U_E} \tag{9}$$

With known geostrophic velocities and wind stress, it is a simple matter to compute **M** from observations but the resulting **M** vector is horizontally divergent and its normal component does not vanish at solid boundaries (since neither normal geostrophic velocities nor Ekman transports do vanish there). Since it is imperative that the time mean barotropic transport be nondivergent, we must correct **M** and find a corrected transport $\mathbf{M}^*$ satisfying

$$\nabla_H\cdot\mathbf{M}^* = 0 \tag{10}$$

Equation (10) assumes stationarity and neglects the forcing by evaporation and precipitation, on account of their small values relative to observed oceanic transports. One way to implement 10 is to find out a barotropic stream function $\psi(\lambda,\theta)$ linked to the initial barotropic transport **M** by

$$\begin{aligned} M_\lambda &= -\frac{1}{r_0}\partial_\theta\psi \\ M_\theta &= \frac{1}{r_0\ \cos\theta}\partial_\lambda\psi \end{aligned} \tag{11}$$

With **M** known from 9, the equation obeyed by ψ in Cartesian coordinates (λ, θ) is simply

$$\frac{\partial^2\psi}{\partial\lambda^2} + \frac{\partial^2\psi}{\partial\theta^2} = r_0[\partial_\lambda(M_\theta\cos\theta) - \partial_\theta(M_\lambda)] \tag{12}$$

the same equation as 4 but forced on the right-hand side by the curl of the vector $\mathbf{m} = (r_0 M_\lambda, r_0\cos\theta M_\theta)$. The difference between the Poisson problems 4 and 12 comes from the boundary condition. If the net mass transport across a zonal section is to vanish, 11 shows that

$$\int_{\lambda_W}^{\lambda_E} M_\theta\ r_0\cos\theta\ d\lambda = \psi(\lambda_E) - \psi(\lambda_W) = 0$$

The no net mass transport implies that the values of the stream function should be identical on each side of the section whose end points are indicated by the longitudes λ_W and λ_E. This is guaranteed if the normal component of the barotropic transport vanishes at the boundaries of the domain. With the coast defined by the equation $F(\lambda, \theta) = 0$, we must have

$$\mathbf{M}^*\cdot\nabla F = 0$$

By inserting 11, this becomes

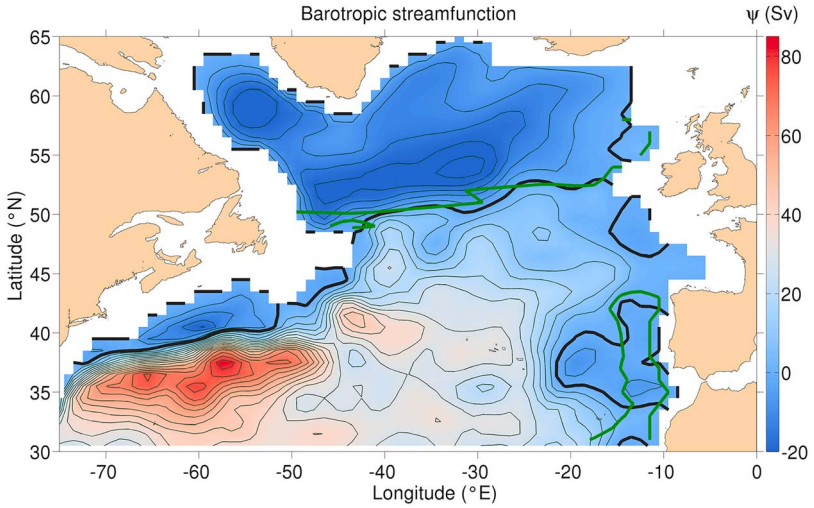

Figure 4. The North Atlantic subpolar gyre barotropic stream function after inversion of the second Poisson problem 12, CI = 5 Sv. The $\psi = 0$ value is given by the bold black contour. The green contour is the $\psi = 0$ value of the Sverdrup stream function.

$$J(\psi, F) = 0 \tag{13}$$

with J the Jacobian operator in (λ,θ) Cartesian coordinates. Obviously, the Jacobian vanishes if ψ is a constant C over the boundary:

$$\psi = C \text{ at } F(\lambda, \theta) = 0 \tag{14}$$

The Poisson equation (12) with boundary condition (14) is of the Dirichlet type and can be solved using the numerical methods described in CVO. Once ψ is known, a corrected, nondivergent barotropic transport $\mathbf{M}^*$ follows from 11.

In the current application to the subpolar North Atlantic gyre, the small islands and regions with not enough data have been filled by interpolation to avoid the complications of a multiply-connected domain. The Bering Strait transport being neglected, the $\psi = 0$ boundary condition can be imposed on both the American and European coasts. Of course barotropic transports at *open* boundaries remain additional assumptions of the present method. No net flow is imposed at the southern open boundary at 5.5°N. Communication with the Arctic occurs with 4.7 Sv leaving the Atlantic at 62.5°N (between 24.5 and 9.5°W) and 4.7 Sv entering the Atlantic at 28.5°W (between 62.5 and 65.5°N) with implementation detailed in CVO. The barotropic stream function for the subpolar gyre is shown in Figure 4. Given an rms error ε_ϕ on the mean geopotential Φ at 1000 dbar $\varepsilon_\phi = g \cdot 10^{-2}$ m, the rms error on ψ becomes $\varepsilon_\psi = \frac{H}{f}\varepsilon_\phi$ using geostrophy or about 4 Sv for $H = 4$ km and $f = 10^{-4}$ s^{-1}. Of course it varies in space with the inverse square root of the number of degrees of freedom (the number of float days in a bin divided by the Lagrangian integral time scale ~10 days). The central feature in Figure 4 is the Gulf Stream jet with a maximum transport of 97.5 Sv at 60°W and flanked to the north and south by the cyclonic and anticyclonic recirculations. The subtropical and subpolar gyres are separated by the $\psi = 0$ contour straddling the latitudes 50–52°N, a separation well predicted by the 0 contour of the Sverdrup stream function. Although the local test of the Sverdrup relation in the subtropical gyre is not good, the subtropical and subpolar gyres are well separated by this line of 0 Sverdrup transport. The southward flow along the eastern flank of the Mid-Atlantic ridge is part of a cyclonic cell found in the eastern basin and is a westward extension of the cyclonic cell of the Mediterranean outflow described by Lamas et al., 2010, east of 14°W. Our position about the validity of Sverdrup balance differs from that of Gray and Riser (2014) who noted good agreement over large areas, primarily in the tropics and subtropics. However, the two studies differ in methods to reconstruct the circulation and dynamical assumptions: while we obtain here top to bottom transports using Argo float displacement and World Ocean Atlas (WOA), they chose instead to integrate meridional geostrophic velocity vertically from the surface over a depth h that minimizes difference with the wind forcing term, the pointwise value of h (the bottom boundary of their calculation) varying in the

range (200 and 1,000 m). While their calculation assumes that vertical velocity vanishes at this depth h, our test assumes that it vanishes at the bottom as demanded by the Sverdrup relation (Pedlosky, 1996).

Step 3: As we now show, the knowledge of the geostrophic velocities $\mathbf{u_G}$ by Step 1 and the knowledge of the nondivergent barotropic transport $\mathbf{M}^*$ and of the Ekman transport by Step 2 allow to determine completely the overturning and the meridional heat transports in the basin. To compute the heat transport, the net meridional transport across the basin must vanish. With boundaries at longitudes λ_W and λ_E, this is:

$$\int_{\lambda_W}^{\lambda_E}\int_{-H}^{0} v\, r_0 \cos\theta \mathrm{d}\lambda \mathrm{d}z = 0 \tag{15}$$

where the meridional velocity v is the sum of geostrophic velocity and Ekman velocity:

$$v = v_G + v_E$$

The Ekman layer is not resolved and the wind stress is imposed as a body force over a mixed layer of 75-m depth, so that v_E is a constant in the mixed layer and 0 below. The traditional method of Bryan (1969) to solve the primitive equations is to decompose the velocity into a barotropic component carrying the total transport and the residual baroclinic component:

$$v = v^+ + v_G^- + v_E^- \tag{16}$$

where the meridional barotropic component is

$$v^+ = \frac{M_\theta^*}{H} \tag{17}$$

and the two baroclinic geostrophic and Ekman components with 0 net transport are simply:

$$\begin{aligned} v_G^- &= v_G - \frac{1}{H}\int_{-H}^{0} v_G \,\mathrm{d}z \\ v_E^- &= v_E - \frac{1}{H}\int_{-H}^{0} v_E \,\mathrm{d}z \end{aligned} \tag{18}$$

The baroclinic velocities are known from thermal wind (in situ density) and the Ekman velocities from wind stress (and the constant mixed layer depth). It is worth to emphasize that relation (18) is *local* to be contrasted with the *global elliptic* character of the relations 4 and 12 to be inverted to obtain the barotropic velocity v^+, the only difficulty of the PGM.

The zonally integrated transport V (the MOC) and the overturning stream function χ are linked at any depth z by

$$V = \int_{\lambda_W}^{\lambda_E} v\, r_0 \cos\theta \,\mathrm{d}\lambda = -\frac{\partial \chi}{\partial z}$$

Using 16 and integrating from the bottom where $\chi(-H) = 0$ gives

$$\chi = -\int_{-H}^{z}\left[\int_{\lambda_W}^{\lambda_E}\left(v^+ + v_G^- + v_E^-\right) r_0 \cos\theta \,\mathrm{d}\lambda\right]\mathrm{d}z \tag{19}$$

Equation (19) shows readily that the second boundary condition on the overturning stream function $\chi(z = 0) = 0$ is met since each part v^+, v_G^- and v_E^- of 19 satisfies the 0 transport condition (15). Following Hall and Bryden (1982), the meridional heat transport is written as

$$Q = \rho_0 C_p \int_{\lambda_W}^{\lambda_E}\int_{-H}^{0}\left(v\,\theta_p\right) r_0 \cos\theta \,\mathrm{d}\lambda \mathrm{d}z \tag{20}$$

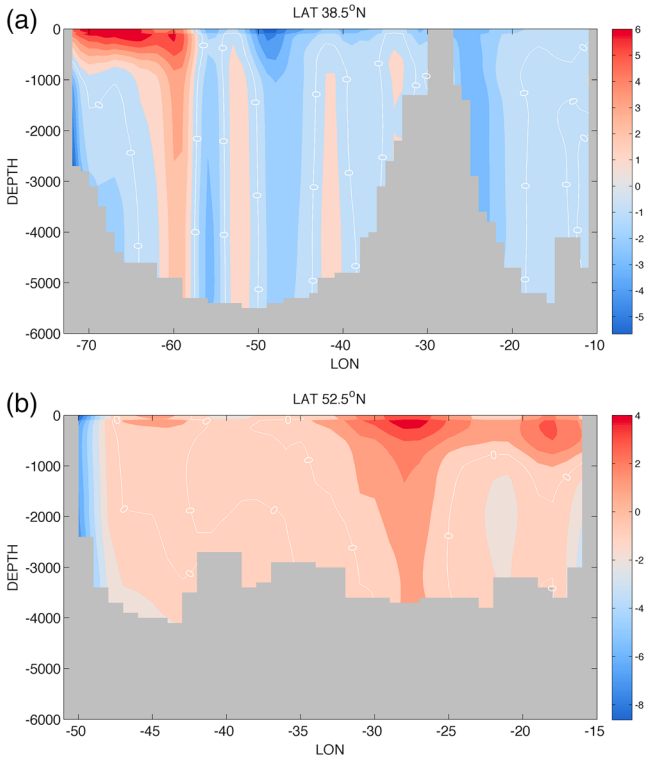

Figure 5. The meridional velocities v reconstructed from 16 that are used for the heat transport calculation. The net transport over the section vanishes. (a) at 38.5°N, (b) at 52.5°N, unit cm/s.

The quantities ρ_0 and C_p are taken out of the integral because of their small variations ($\rho_0\, C_p = 4.07 \cdot 10^6$ J·m^{-3}·K^{-1}) and the variable θ_p is the potential temperature (referenced to the surface). Introducing the vertical mean temperature and perturbations

$$\theta_p^+ = \frac{1}{H}\int_{-H}^{0} \theta_p \mathrm{d}z$$
$$\theta'_p = \theta_p - \theta_p^+$$

Using 16, the heat transport 20 can be written finally as

$$Q = \rho_0 C_p \int_{\lambda_W}^{\lambda_E} \left[M_\theta^* \, \theta_p^+ + \int_{-H}^{0} \left(v_G^- \, \theta'_p + v_E^- \, \theta'_p \right) \mathrm{d}z \right] r_0 \cos\theta \, \mathrm{d}\lambda \tag{21}$$

It is interesting to compare this determination with the heat transport carried out by the MOC itself which is simply the vertical integral of the product of the zonally integrated v and θ_p:

$$Q_{\mathrm{MOC}} = \rho_0 C_p \int_{-H}^{0} V \, \Theta \, \mathrm{d}z$$
$$\text{with} \quad \Theta = \int_{\lambda_W}^{\lambda_E} \theta_p \, r_0 \cos\theta \mathrm{d}\lambda \tag{22}$$

Equation (21) shows the three contributions of the barotropic, baroclinic geostrophic, and Ekman velocities to the heat transport. The difficulty has always been the first term, the barotropic contribution. If θ_p^+ varies weakly with longitude (which is true of certain latitudes with small bottom variations), 15 shows that this barotropic contribution is small. On the contrary, Hall and Bryden (1982) demonstrated its importance at

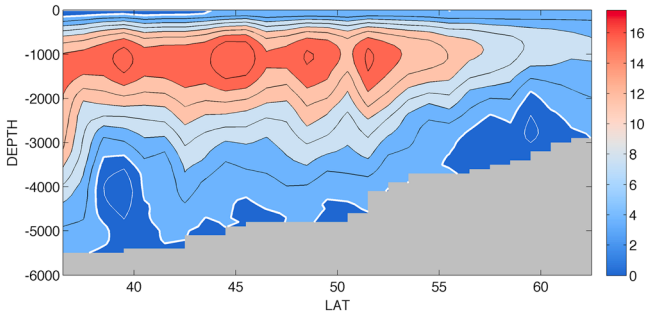

Figure 6. The total overturning stream function (Sv) as a function of latitude and depth. The $\chi = 0$ contour is given by the bold white contour. Positive (negative) values are given by the thin black (white) contours, CI = 2.5 Sv.

24°N as the Florida Current flows over a shallow region of large θ_p^+ while the return flow in the interior occurs over abyssal plains with a much smaller θ_p^+.

Given the importance of the meridional velocities in 21, the reconstructed total velocities given by 16 are now shown at two latitudes in Figure 5. At 38.5°N, the major features are the western boundary current that reaches the bottom at 60°W and the southward flow of deep water also trapped over the western boundary. Two major regions of surface intensified southward flow are located at 48°W and around 25°W east of the Mid-Atlantic ridge. At 52.5°N the main features are the bottom reaching North Atlantic drift at 27°W and the nearly barotropic southward western boundary current (i.e., the Labrador Current). There is also a net northward flow closer to the eastern boundary around 17°W.

3. The Overturning and Heat Transport of the Subpolar North Atlantic Gyre

3.1. (i) The Overturning

The overturning stream function χ computed from 19 is shown in Figure 6. Since the overturning is obtained in part from a zonal average of barotropic velocities, we expect the error to be smaller than the 4 Sv error on the individual barotropic velocities. The standard error on the overturning is reduced by a factor $1/\sqrt{N}$ with N the number of degrees of freedom, tentatively estimated from the number of grid points $N \sim 30$ at the 1° scale (an eddy scale), yielding ~ 0.7 Sv. This can be considered a lower bound because of the remaining spatial correlations at lag greater than 1°. The poleward moving surface limb that extends to 1,000 m is nearly constant up to 52°N. The maxima occur between 1,000 and 1,500 m with rates of 18.5, 19.6, and 18 Sv at 40, 45, and 51°N, respectively, and reducing to 7 Sv at 60°N. These values are 10 to 15% higher than those of Lumpkin and Speer (2007) and Ganachaud and Wunsch (2000) in Table 1. To compare with other studies, the transport computed across a Portugal (10.5°W–40.5°N)-Greenland (44.5°W–57.5°N) section reaches 18.5 Sv significantly higher than the inverse modeling values, ~10 Sv for the 2002 OVIDE section and ~ 13.5 Sv for the WOCE A25 FOUREX section (Lherminier et al., 2007), but of the same order as their determinations with respect to density as summarized by Mercier et al. (2015). Our Portugal-Greenland estimate is in line with the 18.4 Sv overturning found by Rossby et al. (2017) on a 2012–2016 repeated section between Greenland and Scotland at 59.5°N where the reference velocity is given by shipboard acoustic Doppler current profiler mounted on a ship of opportunity. The description of the circulation of the subpolar gyre as impacted by the OVIDE observations is found in Daniault et al. (2016).

Table 1
The Heat Transport in the Subpolar Atlantic as Measured by Different Investigators at Different Latitudes, Unit PW

Latitude	Authors	Observations	(PW)	PGM heat transport (PW)	PGM overturning (Sv)
36°N	Sato and Rossby (2000)	CTD sections	1.2	0.47	16.2
	Roemmich and Wunsch (1985)	CTD section 1981	0.8		
	Rintoul and Wunsch (1991)	CTD section 1981	1.3		
	Talley (2003)	CTD section, Reid velocities	0.86		
	McDonagh et al. (2010)	CTD section, 2005	1.14		
41°N	Hobbs and Willis (2012)	Argo floats, SSH	0.5	0.51	16.5
47–48°N	Ganachaud and Wunsch (2000)	WOCE CTD sections 1993	0.6	0.37	15.7
	Koltermann et al. (1999)	CTD sections 1982 and 1993	0.62 and 0.53		
	Talley (2003)	CTD section, Reid velocities	0.62		
	McDonald and Wunsch (1996)	WOCE CTD sections 1993	0.7		
	Lumpkin et al. (2008)	5 CTD sections WOCE AR19 from 1993 to 2000	0.5 to 0.55		
55°N	Bacon (1997)	CTD section Greenland-Ireland	0.28	0.39	13.9

Note. The heat transport and overturning found here are given in the last two columns. PGM = Planetary Geostrophic Method; WOCE = World Ocean Circulation Experiment.

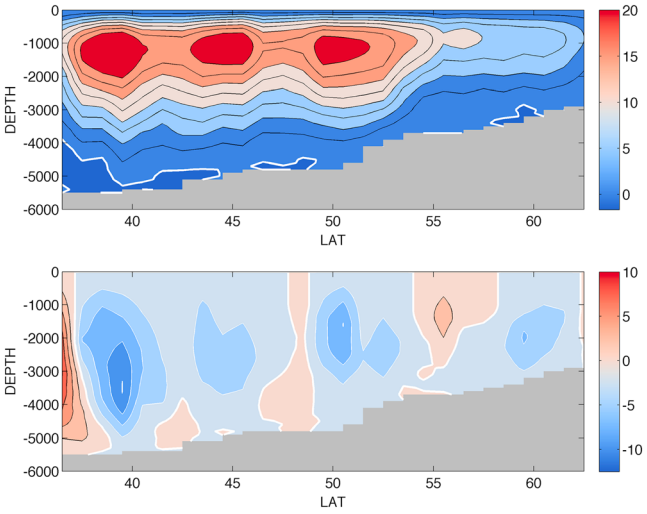

Figure 7. The baroclinic part (top) and barotropic part (bottom) of the overturning stream function (Sv) as a function of latitude and depth. The $\chi = 0$ contour is given by the bold white contour. Positive (negative) values are given by the thin black (white) contours, CI = 2.5 Sv.

The barotropic and baroclinic contributions to the overturning from 19 are shown in Figure 7. The weakest contribution of the Ekman cell is not shown (less than 2.5 Sv and barely visible at the surface of Figure 6). Unsurprisingly, the comparison of Figures 6 and 7 shows that the largest contribution comes from the baroclinic velocity. If the bottom was flat, the barotropic part would vanish under steady state but this is not the case here with anomalies of the order of 5 Sv. The barotropic signal occurs with several cells with maxima below 2,000 m that oppose the baroclinic component. There are also cells centered around 48 and 55°N in phase with the baroclinic cells. On the whole we observe that the barotropic contributions tend to smooth out the baroclinic signal (decreasing the amplitude where it is strong and increasing it where it is weaker). Figure 8 shows the meridional transports as a function of depth at three selected latitudes in order to compare with values obtained from the inversion of hydrographic sections by Roemmich and Wunsch (1985) and McDonagh et al. (2010) at 36.5°N, Koltermann et al. (1999) and Lumpkin et al. (2008) at 48.5°N, and Bacon (1997) at 55.5°N, respectively, in Table 1. At 36.5°N even though the maximum of the cumulated transport is roughly similar, the depth distribution is different: The present method gives smaller values near the surface but twice larger values at 500 m, and the northward flow at the bottom is also absent at this latitude. The dip of the overturning contours at latitudes less than 35.5°N and at depth greater than 1,500 m implies surprisingly negative vertical velocities in Figure 6. The zonal sections of the meridional velocities at these latitudes differ mostly from the higher-latitude sections by a strong barotropic Gulf Stream signal extending to the bottom at the westernmost grid point of our model reconstruction. The lack of spatial resolution and the proximity of the Blake plateau (where the barotropic transport is imposed) are probably responsible for a spurious barotropic adjustment of the solution there. At 48.5°N the overturning of 17.5 Sv is in the upper range of the estimates given by the authors for the five sections carried out in the 1993–2000 period. The agreement here may come from the weak contribution of the barotropic transport at this latitude (see Figure 4).

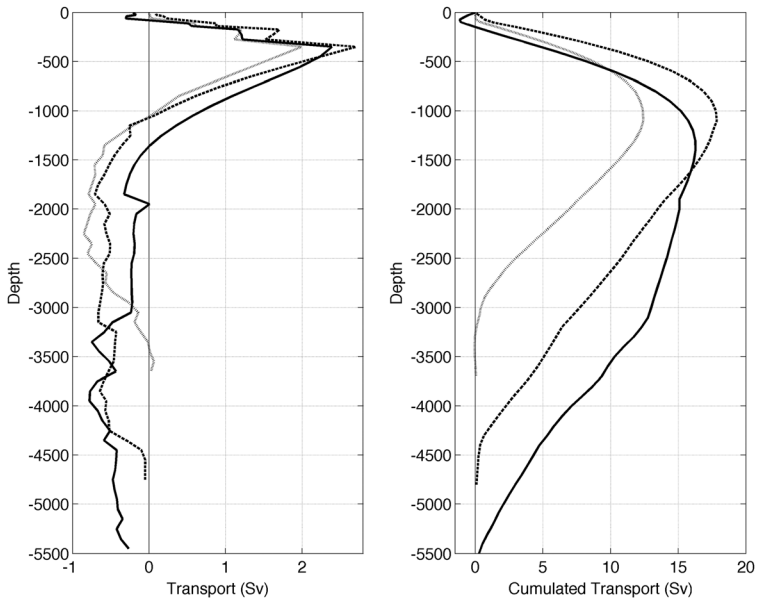

Figure 8. The net meridional transport as a function of depth (left) at 36.5°N (plain), 48.5°N (dashed), and 55.5°N (gray dotted) and their cumulated transport (right), unit Sv.

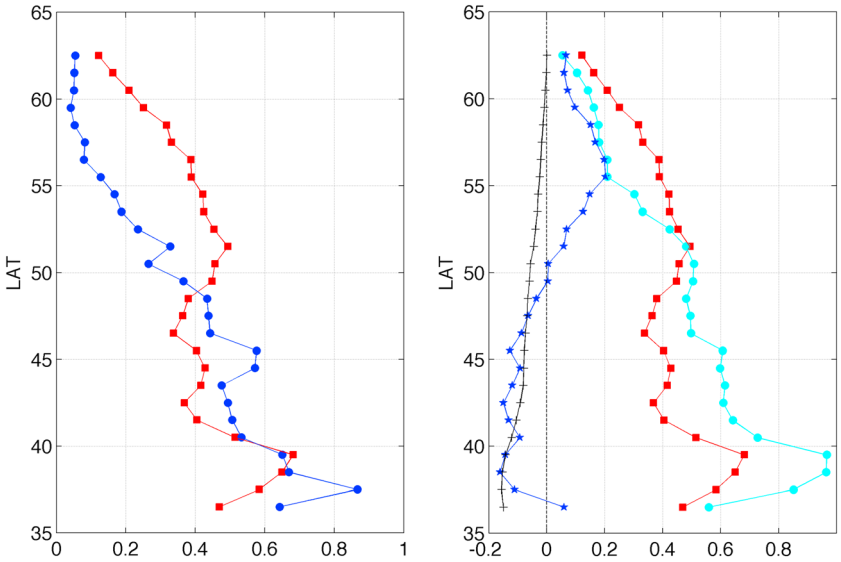

Figure 9. (left) The total meridional heat transport as function of latitude is given by the square red symbols. The heat transport carried out by the overturning (MOC) is given by the blue circles. (right) The total meridional heat transport as function of latitude (square red symbols) and its various parts: the barotropic, baroclinic, and Ekman contributions are shown with blue stars, cyan circles, and black +, respectively. Units petawatt: 1 PW = 10^{15} W.

3.2. (iv) The Meridional Heat Fluxes

Each of the barotropic, baroclinic, and Ekman contributions computed from 21 and the MOC contribution from 22 are shown in Figure 9. Focusing again on errors associated with the variance of the flow, we estimate the order of magnitude of the error on the heat flux as $4 \cdot 10^6\ \mathrm{J{\cdot}m^{-3}\cdot K^{-1}} \times 0.7 \cdot 10^6\ \mathrm{m^3/s} \times \theta_p^+ (= 5\ ^\circ\mathrm{C}) \sim 1.4 \cdot 10^{-2}$ PW, about an order of magnitude smaller than the signal of Figure 9. At latitudes less than 48°N, the MOC transport overestimates the total heat transport by ~ 0.1 PW but underestimates it by up to 0.3 PW at higher latitudes, a relative error of more than 50%. The idea of a two dimensional (latitude-depth) thermohaline circulation providing the meridional heat transport fails in the Atlantic subpolar gyre as the horizontally varying anomalies contribute significantly to the heat transport. Turning now to the decomposition 21, we first note that the Ekman contribution to the heat transport is negative. Because the Ekman transport is southward, the baroclinic Ekman cell, southward at the surface and northward at depth, generates a negative heat transport in the subpolar gyre. Its amplitude decreases to become negligible north of 50°N because the westerlies weaken and the Coriolis parameter f increases. We find that the major contribution to the heat transport comes from the baroclinic geostrophic velocities. The baroclinic term overestimates the total heat flux for latitudes less than 48°N and underestimates it beyond because of the presence of the barotropic contribution and Ekman contribution: The barotropic and Ekman heat transports are negative south of 48°N and oppose the positive baroclinic transport. North of 50°N the barotropic contribution becomes positive and reinforces the baroclinic. The sign of the barotropic contribution to heat transport can be rationalized as follows: The barotropic flow acts on the vertically averaged temperature θ_p^+ that is cold in the west and larger in the east. This temperature gradient is not caused by topographic differences but is a response to the circulation. At latitudes less than 48°N, the anticyclonic barotropic cell associates a poleward boundary current with cold temperature θ_p^+ while the southward flow returns with higher θ_p^+, making an overall negative heat flux contribution. This is the opposite at latitudes beyond 48°N, the cyclonic barotropic cell now transports warmer eastern basin water to the north while the southward return flow in the western region is associated with colder water making now a net positive contribution to heat transport. The recent results of the Ocean Subpolar North Atlantic Program by Lozier et al. (2019) confirm the importance of the horizontal circulation for the poleward heat transport.

Most of previous estimates given in Table 1 originate from hydrographic observations with inverse modeling to determine the reference velocity. At 36°N, our estimate is about half the hydrographic values but Figure 9

shows that our estimate increases rapidly with latitudes from 36 to 40°N. The baroclinic part is of the order of the hydrographic estimates, and it is the negative contributions of the barotropic and Ekman velocities that lower significantly our estimate in this latitude range. The southward flow present east of the Mid-Atlantic ridge (visible in Figure 5a) contributes to reduce the heat transport. Of course, this could be a transient feature but it is determined by an average of 200 days of Argo float velocities per 1° × 1° bin in the domain (34–39°N, 20–30°W). At 41°N, our estimate is the same as Hobbs and Willis (2012) who used a combination of altimetric sea surface heights and Argo float for the temperature-salinity profiles. At 47–48°N our estimate is again smaller than the hydrographic estimates by roughly 20–30%. At 55°N our estimate is larger than that of Bacon (1997) but the latter is a Greenland-Ireland section that ignores the western basin contribution.

It is difficult to be very specific about the origin of the differences between our estimates and the inverse modeling hydrographic estimates because of two major differences, the observations and the methodology:

1/We determine the heat transport of a *time mean* circulation with observations spread over 5 years or more whereas past estimates are based on individual hydrographic sections carried out usually over 1- or 2-month time.

2/The method to find the reference velocity differs, direct observation of the reference level velocity by the Argo floats versus inverse modeling. The inverse models are underdetermined, and a solution is obtained through minimization of the distance of the solution to a first guess and therefore relies on the choice of that first guess. The other assumptions are the various conservation laws imposed for the tracers.

If it is impossible to disentangle the two reasons behind the origin of differences in Table 1, it is possible to check whether our heat transport estimates are consistent with the climatology of *mean* surface heat fluxes. Our net heat transport decreases from 0.59 PW at 40°N to 0.23 PW at 60°N, a difference that provides an average flux from ocean to atmosphere of 0.36 PW or 48 W/m^2. This compares well with the 54 W/m^2 that we computed from the air-sea flux data set of Large and Yeager (2009) over the same latitudinal band. This average heat flux provided by the oceanic circulation is used to develop the activity of the storm track in the atmosphere.

4. Conclusion

The new method presented here allows the determination of *mean* oceanic heat transports and overturning from observations using dynamically consistent consequences of the geostrophic assumptions. It is direct and does not use the minimization procedures that are central in inverse modeling. The absolute circulation over whole oceanic basins can be obtained, an objective achieved by the rising Argo float displacement database. Applied to the subpolar North Atlantic, the observed mean overturning reaches 16–18 Sv in the 40–50°N range for the period 2000–2009. The drop in oceanic heat flux from 40 to 60°N leads to a reasonable average air-sea flux of ~50 W/m^2 from ocean to atmosphere that feeds the activity of the storm track. We find that 1/the heat transport cannot be explained by the sole transport of the zonally averaged flow (the MOC), and 2/the barotropic component becomes a significant contribution to the heat transport north of 55°N.

The method, however, does not come without its own difficulties. The low spatial resolution of 1° needs improvement but early tests with higher resolution showed that the mean fields were too contaminated by remaining mesoscale structures. The solution to that problem comes from the increase of the number of degrees of freedom with the float displacement data still to be taken into account. We expect to reach 1/2° resolution by adding the 2010–2018 data to the ANDRO database. The lack of sampling of shelves shallower than the 1,000-m Argo float nominal level is also troublesome. The present subpolar North Atlantic estimates neglect entirely what happens on these shelves. Without the addition of specific velocity measurements on the shelves, nothing can be said of the barotropic contribution. However, the baroclinic velocity contribution to the heat transport including these shelves is easily computed from the WOA data and has been compared with the previous estimate (without the shelves). We find an rms difference of the two estimates of 0.015 PW over the basin, an order of magnitude smaller than the values of Figure 9. However, at 59–60°N latitudes the baroclinic heat transport with the inclusion of the shelves is reduced by up to 20%.

To lower the uncertainties associated with inverse modeling, alternative projects have added direct measurements of the reference velocities along with Conductivity, Temperature, Depth (CTD) observations at a given latitude. The RAPID experiment implemented moorings arrays over selected parts of the section at

26°N (Johns et al., 2011). The international Ocean Subpolar North Atlantic Program followed at 58°N providing a range of current meter and CTD mooring observations and increasing the spatial resolution where necessary with due concern for topographic variations (see Holliday et al., 2018). The OVIDE Program has added similar selected current meter arrays over the Reykyanes ridge and the Greenland coast to constrain the circulation and heat transport over the OVIDE CTD section (Mercier et al., 2015).

By way of comparison the advantage of the present method is to offer a basin-scale view of the time-mean circulation. However, to discuss the Florida Current and the subtropical gyre, it will be necessary to complement the interior Argo float arrays with observations (current meter arrays and ships of opportunity) over selected shallow areas. Once the circulation over the potentially important shallow regions is sampled, we can be confident that the determination of decadal trends of climate change of circulation and heat transports in midlatitude oceanic basins will become possible in a foreseeable future given the continuing flux of Argo float observations.

Acknowledgments
The float data were collected and made freely available by the International Argo program and the National programs that contribute to it (http://argo.jcommops.org). The Argo Program is part of the Global Ocean Observing system. The world deep displacement data set ANDRO used herein has been produced from the Argo float data. One important feature is that the pressures measured during float drifts at depth and suitably averaged are preserved in ANDRO. It can be accessed freely at https://www.seanoe.org/data/00360/47077. The World Ocean Atlas 2009 has been prepared by the National Center for Environmental Information from NOAA. It can be accessed freely at https://www.nodc.noaa.gov/OCS/WOA09/pr_woa09.html The postdoctoral support of T. Meunier by Service Hydrographique et Océanographique de la Marine (SHOM) is gratefully acknowledged. Three anonymous reviewers are warmly thanked for their questions, comments and careful editing which improved the paper. Many thanks to O. Arzel, T. Huck and F. Sévellec for comments on an early draft of this paper.

References

Antonov, J. I., Seidov, D., Boyer, T. P., Locarnini, R. A., Mishonov, A. V., Garcia, H. E., et al. (2010). World Ocean Atlas 2009. In S. Levitus (Ed.), *Salinity*, NOAA Atlas NESDIS 69 (Vol. 2, 184 pp.). Washington, D.C: U.S. Government Printing Office.

Argo, 2000, Argo float meta data from Global Data Assembly Centre (Argo GDAC). SEANOE. http://doi.org/10.17882/42182.

Bacon, S. (1997). Circulation and fluxes in the North Atlantic between Greenland and Ireland. *Journal of Physical Oceanography*, *27*(7), 1420–1435. https://doi.org/10.1175/1520-0485(1997)027<1420:CAFITN>2.0.CO;2

Bryan, K. (1962). Measurements of meridional heat transports by ocean currents. *Journal of Geophysical Research*, *67*(9), 3403–3414. https://doi.org/10.1029/JZ067i009p03403

Bryan, K. (1969). A numerical method for the study of the circulation of the World Ocean. *Journal of Computational Physics*, *4*(3), 347–376. https://doi.org/10.1016/0021-9991(69)90004-7

Bryden, H. L., & Imawaki, S. (2001). Ocean Heat transport. In G. Siedler, J. Church, & J. Gould (Eds.), *Ocean circulation and climate* (pp. 455–474). London: Academic Press.

Bryden, H. L., Roemmich, D. H., & Church, J. A. (1991). Ocean heat transport across 24°N in the Pacific. *Deep Sea Research Part A. Oceanographic Research Papers*, *38*(3), 297–324. https://doi.org/10.1016/0198-0149(91)90070-v

Charney, J. (1955). The use of primitive equations of motion in numerical prediction. *Tellus*, *7*(1), 22–26.

Colin de Verdière, A., & Ollitrault, M. (2016). A direct determination of the World Ocean barotropic circulation. *Journal of Physical Oceanography*, *46*(1), 255–273. https://doi.org/10.1175/JPO-D-15-0046.1

Daniault, N., Mercier, H., Lherminier, P., Sarafanov, A., Falina, A., Zunino, P., et al. (2016). The northern North Atlantic Ocean mean circulation in the early 21st century. *Progress in Oceanography*, *146*, 142–158. https://doi.org/10.1016/j.pocean.2016.06.007

Davis, R. E. (1991). Observing the general circulation with floats. *Deep Sea Research Part A. Oceanographic Research Papers*, *38*(suppl. 1), 531–572.

Davis, R. E., Webb, D. C., Regier, L. A., & Dufour, J. (1992). The Autonomous Lagrangian Circulation Explorer (ALACE). *Journal of Atmospheric and Oceanic Technology*, *9*(3), 264–285. https://doi.org/10.1175/1520-0426(1992)009<0264:TALCE>2.0.CO;2

Ganachaud, A., & Wunsch, C. (2000). Improved estimates of global ocean circulation, heat transport and mixing from hydrographic data. *Nature*, *408*(6811), 453–457. https://doi.org/10.1038/35044048

Gent, P., & McWilliams, J. C. (1983). Regimes of validity for balanced models. *Dynamics of Atmospheres and Oceans*, *7*(3), 167–183. https://doi.org/10.1016/0377-0265(83)90003-9

Gray, A. R., & Riser, S. C. (2014). A global analysis of Sverdrup balance using absolute geostrophic velocities from Argo. *Journal of Physical Oceanography*, *44*(4), 1213–1229. https://doi.org/10.1175/JPO-D-12-0206.1

Hall, M. M., & Bryden, H. L. (1982). Direct estimates and mechanisms of ocean heat transport. *Deep Sea Research Part A. Oceanographic Research Papers*, *29*(3), 339–359. https://doi.org/10.1016/0198-0149(82)90099-1

Hobbs, W. R., & Willis, J. K. (2012). Midlatitude North Atlantic heat transport: A time series based on satellite and drifter data. *Journal of Geophysical Research*, *117*, C01008. https://doi.org/10.1029/2011JC007039

Holliday, N. P., Bacon, S., Cunningham, S. A., Gary, S. F., Kartensen, J., King, B. A., et al. (2018). Supolar North Atlantic overturning and gyre scale circulation in the summers of 2014 and 2016. *Journal of Geophysical Research: Oceans*, *123*, 4538–4559. https://doi.org/10.1029/2018JC013841

Huck, T., Weaver, A., & Colin de Verdière, A. (1999). On the influence of the parameterization of lateral boundary layers on the thermohaline circulation in coarse-resolution ocean models. *Journal of Marine Research*, *57*(3), 387–426. https://doi.org/10.1357/002224099764805138

Johns, W. E., Baringer, M. O., Beal, L. M., Cunningham, S. A., Kanzow, T., Bryden, H. L., et al. (2011). Continuous, array–based estimates of Atlantic ocean heat transport at 26.5°N. *Journal of Physical Oceanography*, *24*, 2429–2449.

Josey, S. A., Kent, E. C., & Taylor, P. K. (1999). New insights into the ocean heat budget closure problem from analysis of the SOC air-sea flux climatology. *Journal of Climate*, *12*(9), 2856–2880. https://doi.org/10.1175/1520-0442(1999)012<2856:NIITOH>2.0.CO;2

Koltermann, K. P., Sokov, A. V., Tereschenkov, V. P., Dobroliubov, S. A., Lorbacher, K., & Sy, A. (1999). Decadal changes in the thermohaline circulation of the North Atlantic. *Deep Sea Research Part II: Topical Studies in Oceanography*, *46*(1-2), 109–138. https://doi.org/10.1016/S0967-0645(98)00115-5

Lamas, L., Peliz, A., Ambar, I., Aguiar, A. B., & Maximenko, N. (2010). Evidence of time-mean cyclonic cell southwest of Iberian Peninsula: The Mediterranean Outflow-driven β plume? *Geophysical Research Letters*, *37*, L12606. https://doi.org/10.1029/2010GL043339

Large, W. G. and S. G. Yeager, 2004: Diurnal do decadal global forcing for ocean and sea-ice models: The data sets and flux climatologies. NCAR Tech. Rep., TN-460 + STR, 122 pp.

Large, W. G., & Yeager, S. G. (2009). Global climatology of an interannually varying air-sea flux data set. *Climate Dynamics*, *33*(2-3), 341–364. https://doi.org/10.1007/s00382-008-0441-3

Lherminier, P., Mercier, H., Goucuff, C., Alvarez, M., Bacon, S., & Kermabon, C. (2007). Transports across the 2002 Greenland-Portugal Ovide section and comparison with 1997. *Journal of Geophysical Research*, *112*, C07003. https://doi.org/10.1029/2006JC003716

Locarnini, R. A., Mishonov, A. V., Antonov, J. I., Boyer, T. P., Garcia, H. E., Baranova, O. K., et al. (2010). World Ocean Atlas 2009. In S. Levitus (Ed.), *Temperature*, NOAA Atlas NESDIS 68 (Vol. 1, 184 pp.). Washington, D.C: U.S. Government Printing Office.

Lozier, M. S., Li, F., Bacon, S., Bahr, F., Bower, A. S., Cunningham, S. A., et al. (2019). A sea change in our view of overturning in the subpolar North Atlantic. *Science*, *363*(6426), 516–521. https://doi.org/10.1126/science.aau6592

Lumpkin, R., & Speer, K. (2007). Global ocean meridional overturning. *Journal of Physical Oceanography*, *37*(10), 2550–2562. https://doi.org/10.1175/JPO3130.1

Lumpkin, R., Speer, K. G., & Koltermann, K. P. (2008). Transport across 48°N in the Atlantic Ocean. *Journal of Physical Oceanography*, *38*(4), 733–752. https://doi.org/10.1175/2007JPO3636.1

Macdonald, A. M., & Baringer, M. O. (2013). Ocean heat transport. In G. Siedler, S. M. Griffies, J. Gould, & J. Church (Eds.), *Ocean circulation and climate: A 21st century perspective*, *International Geophysics Series* (Vol. 103, pp. 759–785). Academic Press. https://doi.org/10.1016/B978-0-12-391851-2.00029-5

Macdonald, A. M., & Wunsch, C. (1996). An estimate of global ocean circulation and heat fluxes. *Nature*, *382*, 436–439. https://doi.org/10.1038/382436a0

Mann, C. R. (1967). The termination of the Gulf Stream and the beginning of the North Atlantic Current. *Deep Sea Research*, *14*, 337–359.

McDonagh, E. L., McLeod, P., King, B. A., & Bryden, H. L. (2010). Circulation heat and freshwater transport at 36°N in the Atlantic. *Journal of Physical Oceanography*, *40*(12), 2661–2678. https://doi.org/10.1175/2010JPO4176.1

Mercier, H., Lherminier, P., Sarafanov, A., Gaillard, F., Daniault, N., Desbruyères, D., et al. (2015). Variability of the meridional overturning circulation at the Greenland-Portugal Ovide section from 1993 to 2010. *Progress in Oceanography*, *132*, 250–261. https://doi.org/10.1016/j.pocean.2013.11.001

Ollitrault, M., & Colin de Verdière, A. (2014). The ocean general circulation near 1000 m depth. *Journal of Physical Oceanography*, *44*(1), 384–409. https://doi.org/10.1175/JPO-D-13-030.1

Ollitrault, M., & Rannou, J. P. (2013). ANDRO: An Argo-based deep displacement dataset. *Journal of Atmospheric and Oceanic Technology*, *30*(4), 759–788. https://doi.org/10.1175/JTECH-D-12-00073.1

Paillet, J., Arhan, M., & McCartney, M. S. (1998). Spreading of Labrador sea water in the eastern North Atlantic. *Journal of Geophysical Research*, *103*(C5), 10,223–10,239. https://doi.org/10.1029/98JC00262

Paillet, J., & Mercier, H. (1997). An inverse model of the eastern North Atlantic general circulation and thermocline ventilation. *Deep Sea Research Part I: Oceanographic Research Papers*, *44*(8), 1293–1328. https://doi.org/10.1016/S0967-0637(97)00019-8

Pedlosky, J. (1996). *Ocean circulation theory*, (p. 453). Berlin, Heidelberg: Springer-Verlag. https://doi.org/10.1007/978-3-662-03204-6

Rintoul, S. R., & Wunsch, C. (1991). Mass, Heat, oxygen and nutrients fluxes and budgets in the North Atlantic Ocean. *Deep Sea Research Part I: Oceanographic Research Papers*, *38*(suppl. 1), S355–S377. https://doi.org/10.1016/S0198-0149(12)80017-3

Roemmich, D., & Wunsch, C. (1985). Two transatlantic sections: Meridional circulation and heat flux in the subtropical North Atlantic Ocean. *Deep Sea Research Part I: Oceanographic Research Papers*, *32*(6), 619–664. https://doi.org/10.1016/0198-0149(85)90070-6

Rossby, T., Reverdin, G., Chafix, L., & SØiland, H. (2017). A direct estimate of poleward volume, heat and freshwater fluxes at 59.5°N between Greenland and Scotland. *Journal of Geophysical Research: Oceans*, *122*, 5870–5887. https://doi.org/10.1002/2017JC012835

Sato, O. T., & Rossby, T. (2000). Seasonal and low frequency variability of the meridional heat flux at 36°N in the North Atlantic. *Journal of Physical Oceanography*, *30*(3), 606–621. https://doi.org/10.1175/1520-0485(2000)030<0606:SALFVO>2.0.CO;2

Stammer, D., Wunsch, C., Giering, R., Eckert, C., Heimbach, P., Marotzke, J., et al. (2002). Global ocean circulation during 1992–1997, estimated from ocean observations and a general circulation model. *Journal of Geophysical Research*, *107*(C9), 1–27. https://doi.org/10.1029/2001JC000888

Stammer, D., Wunsch, C., Giering, R., Eckert, C., Heimbach, P., Marotzke, J., et al. (2003). Volume, heat and freshwater transports of the global ocean circulation 1993–2000, estimated from a general circulation model constrained by World Ocean Circulation Experiment (WOCE) data. *Journal of Geophysical Research*, *105*(C1), 3007. https://doi.org/10.1029/2001/JC001115

Talley, L. D. (2003). Shallow, intermediate and deep overturning components of the global heat budget. *Journal of Physical Oceanography*, *33*(3), 530–560. https://doi.org/10.1175/1520-0485(2003)033<0530:SIADOC>2.0.CO;2

Trenberth, K. E., & Caron, J. (2001). Estimates of meridional atmosphere and ocean heat transports. *Journal of Climate*, *14*(16), 3433–3443. https://doi.org/10.1175/1520-0442(2001)014<3433:EOMAAO>2.0.CO;2

Trenberth, K. E., & Solomon, A. (1994). The global heat balance: Heat transports in the atmosphere and ocean. *Climate Dynamics*, *10*(3), 107–134. https://doi.org/10.1007/BF00210625

Wunsch, C. (1978). The North Atlantic circulation west of 50°W determined by inverse methods. *Reviews of Geophysics and Space Physics*, *16*(4), 583–620. https://doi.org/10.1029/RG016i004p00583

Wunsch, C. (1996). *The ocean circulation inverse problem*, (p. 442). Cambridge: Cambridge University Press. https://doi.org/10.1017/CBO9780511629570